Supplement of Atmos. Chem. Phys., 25, 7527–7542, 2025
https://doi.org/10.5194/acp-25-7527-2025-supplement

Atmospheric Chemistry and Physics
Open Access
EGU

Supplement of

Exploring the aerosol activation properties in coastal shallow convection using cloud- and particle-resolving models

Ge Yu et al.

Correspondence to: Xiaoming Shi (shixm@ust.hk)

Supplementary Information

S1 The basic environmental variables and selected parcel trajectories in the CM1 experiment

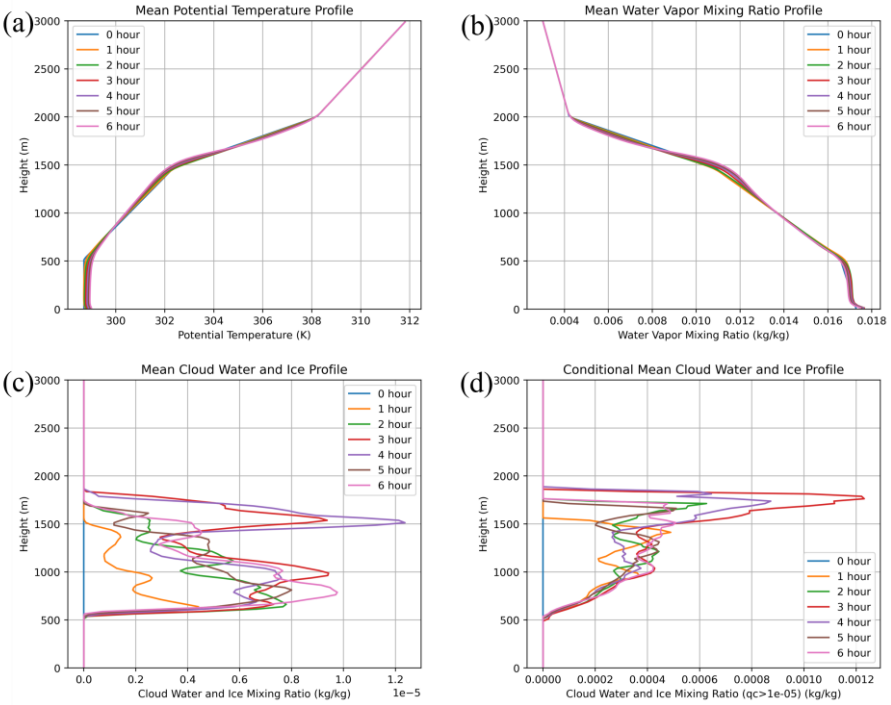

Figure S1. Temporal evolution of horizontal-averaged (a) potential temperature, (b) water vapor mixing ratio, and (c) cloud water and ice mixing ratio with the height in the preliminary CM1 experiment. Panel (d) depicts the conditional mean cloud water and ice mixing ratio over the cloud core (defined as regions where the cloud water mixing ratio exceeds 10^{-5} kg/kg).

Shallow cumulus convections commonly occur in the coastal areas, particularly around midday in the summer. Using the LES simulation in CM1, we simulated an ideal shallow cumulus convection weather condition and tracked the movement of air parcels under it. The vertical distributions of potential temperature and water vapor mixing ratio, as depicted in Fig. S1, exhibit relative stability, highlighting the differentiation between the boundary layer and the free troposphere. In this process, clouds and ice clouds gradually form between 500 m and 2000 m and most of the tracked air parcels tend to move within 2000 m.

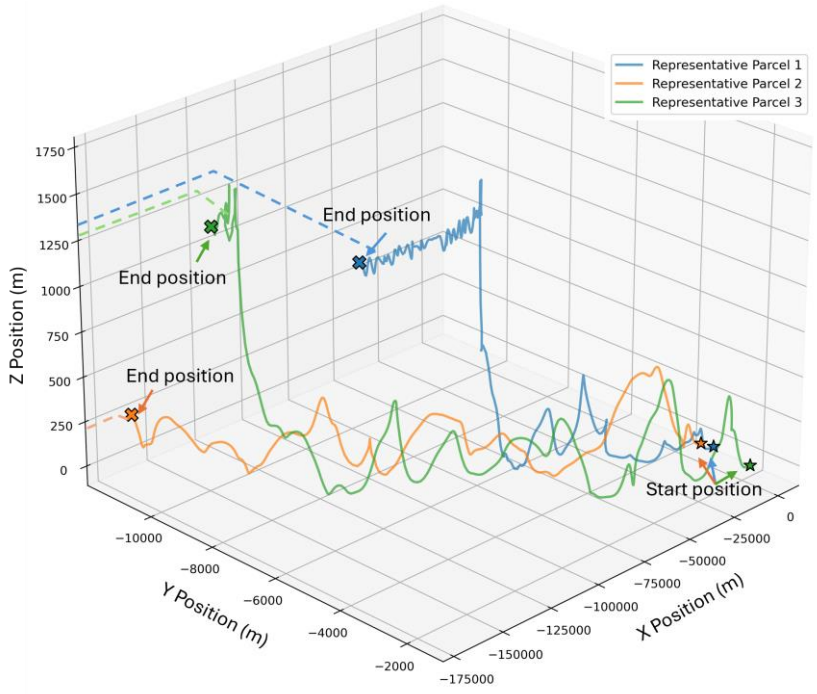

Figure S2. Three-dimensional trajectories of three representative air parcels simulated by the CM1 model. The x and y positions of the parcels have been adjusted to account for the horizontal periodic boundary conditions of the simulation domain, ensuring continuous trajectories across domain boundaries.

The presentation of Fig. S1 is to illustrate the potential cloud formation heights under the typical shallow cumulus convection conditions. As stated in the main text, approximately one-third of the air parcels ascend to altitudes exceeding 1000 meters, where clouds could form. Figure S2 shows three representative parcel trajectories simulated using CM1. In this case, there is an initial background wind speed of approximately 8 m/s in the -x direction. The x and y positions of the air parcels have been adjusted to eliminate discontinuities arising from the horizontal periodic boundary conditions of the simulation domain. The trajectory plot includes both rapidly ascending parcels (with varying ascent timings) and a parcel that remains predominantly within the boundary layer. The ascent of air parcels is rapid, leading to significant environmental changes during this period. Temperature, pressure, and other information extracted from the CM1 simulation are utilized for subsequent PartMC-MOSAIC simulations. The plots also highlight the significance of scenario design in our study. We aim to obtain air parcels at corresponding heights where clouds can form to assess the aerosol evolution processes and the particles' cloud-forming potential.

S2 Detailed changes in the chemical composition during the updraft period

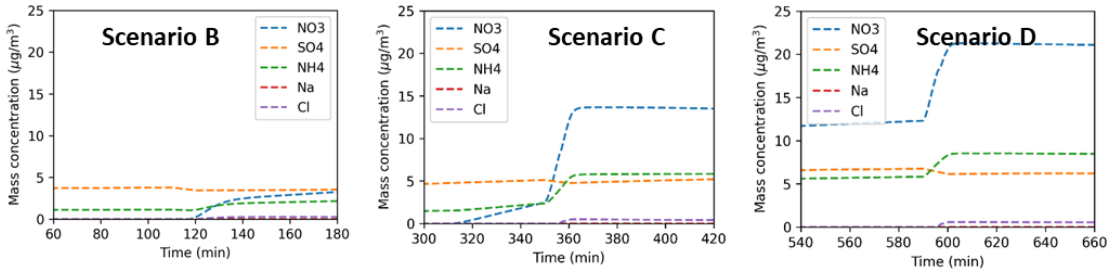

Figure S3. Mass concentration variations of the aerosol inorganic components during the two hours around the parcel updraft in Scenario B, Scenario C, and Scenario D.

In subsection 3.1, we presented the mass variations of aerosol chemical components in different scenarios. Due to the 24-hour simulation period, some high-resolution temporal changes may be lost in Fig. 1. In this part, we supplement the results by providing specific plots during the two hours surrounding the parcel ascent in Scenarios B, C, and D. As shown in Fig. S3, chemical compositions have undergone continuous changes over several minutes rather than a sudden change. The significant increase of nitrate and ammonium corresponds to the time when the parcel leaves the ground. The immediate ascent of the parcel has a large effect on the environmental factors, including temperature, pressure, relative humidity, and emission conditions.

In Scenarios C and D, the increasing trend of specific substances appears more intense than in Scenario B. This phenomenon is due not only to pollutant accumulation but also to the influence of solar effects. The changes associated with the sunlight are evident in the basic case, Scenario A, where the mass concentration of the nitrate rapidly increases after 11 a.m. Aside from the results in Fig. 1, the variation of related gases is also analyzed during the same period. Due to solar effects, the active oxidizing gas ozone may undergo significant changes during the daytime. In our background setup, the parcel in Scenario B departs the ground before 8 a.m., while the impacts of sunlight become apparent after 9 a.m. As a result, in Scenario B, the gases and aerosols remaining in the parcel could have a large difference from the ones in other scenarios.

S3 The comparisons of number-size distribution

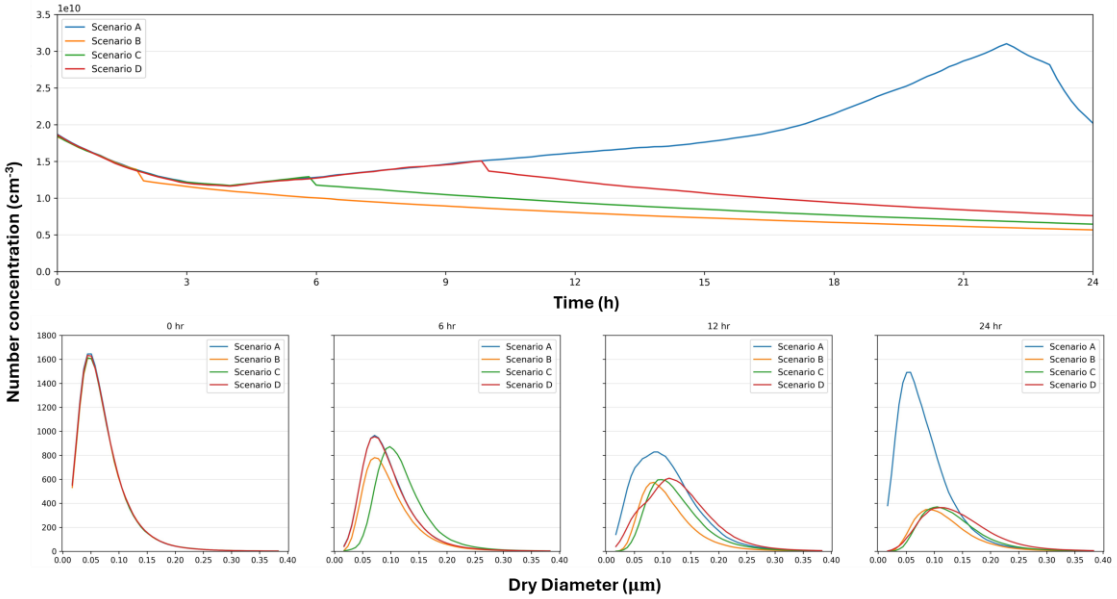

Figure S4. Time series of the total number concentration and the number size distribution of the particles at the selected time in Scenarios A, B, C, and D.

Figure S4 shows the temporal changes in the total number concentration and the size distribution in every scenario at the selected time. The blue, orange, green, and red curves represent the simulated number distributions for Scenario A, B, C, and D, respectively. It can be observed that in Scenario A, the total number concentration of the particles exhibits a descending trend until the 4th hour, after which it steadily increases until the 22nd hour. The descending period coincides with an elevation in the mixing height, indicating a more pronounced dilution effect. In the other scenarios, there is a small sharp decline in the total number concentration of particles during the rapid ascent of the parcel. This is because the parcel expands with the change in pressure and temperature, leading to a sudden decrease in the concentration of aerosols. Meanwhile, there are no longer emissions being introduced, and the surrounding aerosol concentration is also lower as these parcels ascend. Due to the cumulative effect of earlier emissions, the parcels that ascend later (Scenario D) have a higher concentration of particles. Under the combined effects of dilution, chemical reactions, and coagulation processes, the overall number concentration of particles is reduced after the updraft period. The mixing states of these three aerosol populations gradually approach stability, which is further discussed in section 4.

At the beginning of the simulation, the size of most of the particles is around 50 nanometers. The plot at the 24th hour demonstrates that in Scenario A, the particles are predominantly concentrated in the smaller size bins due to the continuous influx of emissions. Fresh emissions primarily consist of small particles, and subsequent aging processes contribute to an increase in both particle size and mass. When the parcels enter the high altitude, the growth regulation of the particle size

varies from the populations near the ground. Gas emissions provide the raw materials for gas-to-particle conversion processes for Scenario B, C, and D. Therefore, at the 12^{th} hour, it is evident that the dominating particles in the parcels with more residential time near the surface tend to have larger diameters. It becomes more prevalent that the size of the particles is around 100 nanometers.

S4 The sensitive impacts of compositions on CCN activation

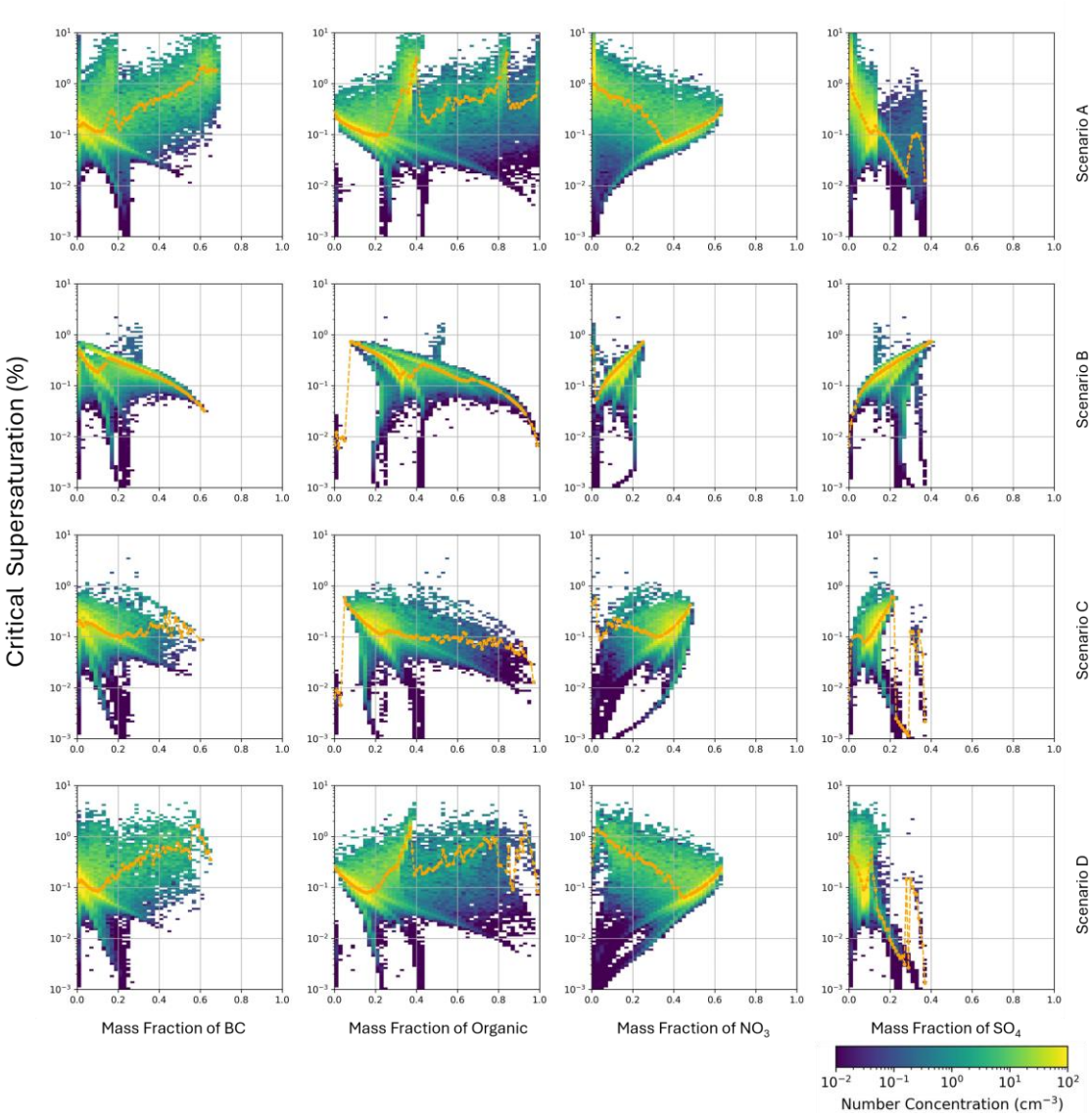

Figure S5. The relationship between the critical supersaturation and mass fractions of black carbon, nitrate, organic matter, and sulfate in aerosols. The figure shows the results for four scenarios on the 12th hour.

Figure S5 illustrates the relationship between the critical supersaturation and mass fractions of several main components in aerosol particles at the 12th hour. Different scenarios are shown in different rows and the color also represents the number concentration of the particles. The orange curves in every subplot depict the median value of the critical supersaturation versus the various mass fractions. In Scenario A, there are two predominant sub-populations with S_c values around 0.1 and 1.0, respectively. In Scenario D, the S_c of most of the particles is around 0.1. The pattern observed in Scenario D resembles that of

Scenario A, except for the second sub-population with a higher S_c. At this stage, the parcel of Scenario D has left the ground for about two hours and the discrepancy primarily arises from the continuous emissions in Scenario A. The distinct sub-population exhibits a low proportion of highly hygroscopic inorganic salt components, including sulfate and nitrate. The characteristics of freshly emitted aerosols are showcased, and they are not prominent in the other scenarios. It is indicated that the aging process may lead to an increased incorporation of inorganic salt components. The particles dominating in Scenario A display a considerable variation in S_c values. As a result, the difference in the CCN activity between the surface parcel and the actual parcel at higher altitudes is not consistently stable within the range of 0.1% to 1% supersaturation. At lower supersaturation levels, a greater number of particles may be activated in the surface parcel. Nevertheless, at higher supersaturation levels, such as 1%, the parcel at higher altitudes exhibits a higher degree of CCN activation.

The trend of the median S_c values (orange curves) reflects the variation in the activation potential of the aerosols as the mass fraction of different substances changes. In general, the S_c values of the particles tend to be lower when they are more prone to be activated. Previous studies have commonly attributed the high hygroscopicity of sulfate components as a key factor in CCN activation. However, the median curves fluctuate without a consistent tendency. With an increase in the mass fraction of sulfate in particles, Scenarios B and C exhibit a rising pattern in the median S_c values. This could be attributed to the influence of particle size. Not only the sort of component but also the size distribution determines the cloud-forming potential of the aerosol populations. Similar inconsistencies are observed in the results for hydrophobic compositions such as BC and organic matter. Despite the increase in mass fraction, the orange curves for organic matter do not exhibit an upward trend, especially for the predominant sub-populations. This finding challenges our conventional understanding. Although it has more organic matter content than other high-concentration aerosols, the particles located in the lower right corner of the yellow region demonstrate a relatively stronger activation potential due to the relatively larger particle sizes. The results may highlight the significant impact brought by the particle sizes. In Scenario B, C, and D, the maximum mass fraction of nitrate increases as the emission accumulates. Furthermore, excluding the freshly emitted particles in scenario A, the trend of the median curve remains uniform across the primary sub-populations in all scenarios. Contrary to expectations, particles with higher nitrate amounts exhibit lower capacity to be activated. This suggests that the nitrate formed during the gas-to-particle conversion process may have a greater tendency to adhere to smaller particles, which is further discussed in Fig. S6.

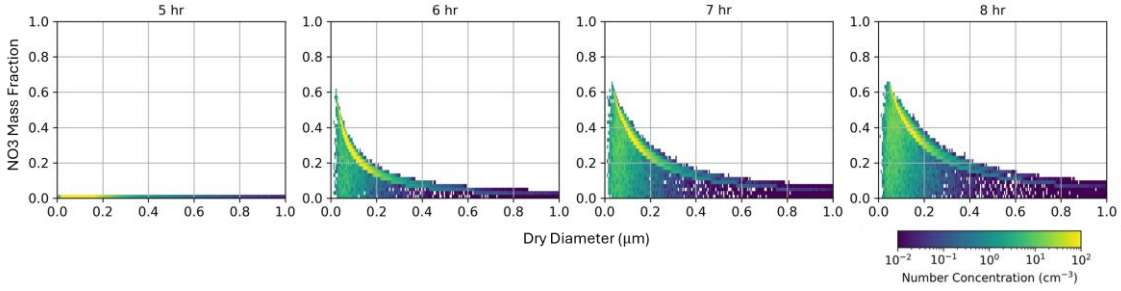

Figure S6. The number concentration distribution of the particles with NO3 mass fraction across particle size at 5~8 hours in Scenario A.

Taking Scenario A as an example, the nitrate component exhibits significant growth from 5 h to 10 h (as shown in Fig. 1). To illustrate the distribution of nitrate within the aerosol population, the relationship between the NO_3 mass fraction and dry diameter at 5 h, 6 h, 7 h, and 8 h for Scenario A is present in Fig. S6. At 5 h, the particles contain negligible amounts of NO_3, while as time progresses, a pronounced increase in NO_3 mass fraction is observed in particles within the smaller size range. In contrast, the growth of NO_3 mass fraction in larger particles demonstrates a more gradual progression. This differential behavior highlights the size-dependent nature of nitrate accumulation in the aerosol population.

S5 The input gas information and horizontal diffusion coefficients for the PartMC simulations

Table S1. The Background and Emission Conditions for Gases

Gas Species	Symbol	Mixing Ratio of the Background Gas (ppb)	Emissions (nmol m^2 s^{-1})
Nitric oxide	NO	0.1	31.8
Nitrogen dioxide	NO_2	1.0	1.67
Nitric acid	HNO_3	1.0	
Ozone	O_3	50.0	
Hydrogen peroxide	H_2O_2	1.1	
Carbon monoxide	CO	21.0	291.3
Sulfur dioxide	SO_2	0.8	2.51
Ammonia	NH_3	0.5	6.11
Hydrogen chloride	HCl	0.7	
Methane	CH_4	2200.0	
Ethane	C_2H_6	1.0	
Formaldehyde	HCHO	1.2	1.68
Methanol	CH_3OH	0.12	0.28
Methyl hydroperoxide	CH_3OOH	0.5	
Acetaldehyde	ALD_2	1.0	0.68
Paraffin carbon	PAR	2.0	96.0
Acetone	AONE	1.0	1.23
Ethene	ETH	0.2	7.2
Terminal olefin carbons	OLET	0.023	2.42
Internal olefin carbons	OLEI	0.00031	2.42
Toluene	TOL	0.1	4.04
Xylene	XYL	0.1	2.41
Lumped organic nitrate	ONIT	0.1	
Peroxyacetyl nitrate	PAN	0.8	
Higher organic acid	RCOOH	0.2	
Higher organic peroxide	ROOH	0.025	
Isoprene	ISOP	0.5	0.23

Alcohols	ANOL	3.45

The gaseous species inputs across all simulation scenarios are systematically cataloged in Table S1. These chemical species align with those documented in Zaveri and Peter (1999), while surface background concentrations and emission parameters were adopted from Riemer et al. (2009). For the background gas concentration at the elevated altitude, we assume no additional substances are introduced into the system. Based on the ideal gas law, the volume mixing ratios of these background trace gases remain constant between the surface and elevated altitudes. Emission rates presented in the table represent temporal averages over emission periods, with actual rates subject to modulation by mixing height variations (Riemer et al., 2009).

Table S2. The Time Series of the Horizontal Dilution Coefficients in Different Scenarios

Scenario	Time (h)	Coefficient (s^{-1})
A	0 ~ 24	1.5×10^{-5}
B	0 ~ 2	1.5×10^{-5}
B	2 ~ 24	3×10^{-6}
C	0 ~ 6	1.5×10^{-5}
C	6 ~ 24	3×10^{-6}
D	0 ~ 10	1.5×10^{-5}
D	10 ~ 24	3×10^{-6}

In Table S2, the displayed time aligns with the temporal scale used for result analysis in the main text, excluding the 6-hour spin-up period. In the 6-hour spin-up PartMC-MOSAIC simulation, the horizontal diffusion coefficients were maintained at 1.5×10^{-5} s^{-1} since the parcels were near the surface throughout the initialization phase.

References:

Riemer, N., West, M., Zaveri, R. A., and Easter, R. C.: Simulating the evolution of soot mixing state with a particle-resolved aerosol model, Journal of Geophysical Research: Atmospheres, 114, https://doi.org/10.1029/2008JD011073, 2009.

Zaveri, R. A. and Peters, L. K.: A new lumped structure photochemical mechanism for large-scale applications, Journal of Geophysical Research: Atmospheres, 104, 30387–30415, https://doi.org/10.1029/1999JD900876, 1999.